Three-phase Evolution of a Coronal Hole. I. 360° Remote Sensing and In Situ Observations

Heinemann, Stephan G.; Temmer, Manuela; Hofmeister, Stefan J.; Veronig, Astrid M.; Vennerstrøm, Susanne

Link back to DTU Orbit

Three-phase Evolution of a Coronal Hole. I. 360° Remote Sensing and In Situ Observations

Stephan G. Heinemann[1] , Manuela Temmer[1] , Stefan J. Hofmeister[1] , Astrid M. Veronig[1] , and Susanne Vennerstrøm[2]
[1] University of Graz, Institute of Physics, Universitätsplatz 5, A-8010 Graz, Austria; stephan.heinemann@hmail.at
[2] National Space Institute, DTU Space, Denmark

Abstract

We investigate the evolution of a well-observed, long-lived, low-latitude coronal hole (CH) over 10 solar rotations in the year 2012. By combining extreme ultraviolet (EUV) imagery from the *Solar TErrestrial RElations Observatories* (*STEREO-A/B*) and the *Solar Dynamics Observatory* (*SDO*), we are able to track and study the entire evolution of the CH having a continuous 360° coverage of the Sun. The remote sensing data are investigated together with in situ solar wind plasma and magnetic field measurements from *STEREO-A/B*, the *Advanced Composition Explorer* (*ACE*), and *WIND*. From this, we obtain how different evolutionary states of the CH as observed in the solar atmosphere (changes in EUV intensity and area) affect the properties of the associated high-speed stream measured at 1 au. Most distinctly pronounced for the CH area, three development phases are derived: (a) growing, (b) maximum, and (c) decaying phase. During these phases the CH area (a) increases over a duration of around three months from about $1 \cdot 10^{10}\,\mathrm{km}^2$ to $6 \cdot 10^{10}\,\mathrm{km}^2$, (b) keeps a rather constant area for about one month of $>9 \cdot 10^{10}\,\mathrm{km}^2$, and (c) finally decreases in the following three months below $1 \cdot 10^{10}\,\mathrm{km}^2$ until the CH cannot be identified anymore. The three phases manifest themselves also in the EUV intensity and in in situ measured solar wind proton bulk velocity. Interestingly, the three phases are related to a different range in solar wind speed variations, and we find for the growing phase a range of 460–600 km s^{-1}, for the maximum phase 600–720 km s^{-1}, and for the decaying phase a more irregular behavior connected to slow and fast solar wind speeds of 350–550 km s^{-1}.

Key words: solar wind – Sun: corona – Sun: heliosphere – Sun: UV radiation

Supporting material: animation

1. Introduction

Coronal holes (CHs) are large-scale structures in the solar corona with one dominant magnetic polarity due to magnetic field lines that do not close within the CH nor within its vicinity. Along those open field lines, plasma can easily escape and radially flow outwards at high speeds (Wilcox 1968). The fast plasma outflow from those localized coronal areas is related to an increased solar wind speed in interplanetary space and referred to as high-speed solar wind streams (HSS). Due to the interaction with the ambient slow solar wind, so-called stream interaction regions are formed. As CHs are long-lived features with lifetimes longer than several solar rotations, these stream interaction regions become corotating interaction regions. At a distance range of 1 au, in situ measurements of the solar wind plasma and magnetic field typically show that the CIR is dominated by a strong bump in the density and magnetic field, followed by a gradual increase in velocity that peaks several days later (Gosling 1996). The production of shocks, compression, and rarefaction regions associated with CIRs are well known sources of recurrent geomagnetic effects on Earth (see, e.g., Alves et al. 2006; Kilpua et al. 2017). Especially during the late declining phase of the solar cycle, CIRs may cause weak to moderate geomagnetic storms (e.g., Verbanac et al. 2011).

Besides their geomagnetic effects, CIRs strongly structure the interplanetary solar wind flow, which has important consequences for the propagation behavior of coronal mass ejections (CMEs) and is one of the key parameters for Space Weather forecasting models. Current solar wind models still have uncertainties in simulating the background solar wind

(see, e.g., Gressl et al. 2014; Jian et al. 2015). Improving our knowledge about the sources of HSS, i.e., the evolution of CHs, is of crucial importance to advance Space Weather forecasting.

CH structures are of low plasma density, and therefore of reduced emission, which makes them observable as dark regions in the extreme ultraviolet (EUV) and X-ray wavelength range (e.g., Schwenn 2006). The identification and extraction is usually based on intensity-threshold methods (Krista & Gallagher 2009; Rotter et al. 2012; Reiss et al. 2014; Hofmeister et al. 2017). The observed CH areas are found to be well correlated with the solar wind speed measured in situ at 1 au (Krieger et al. 1973; Nolte et al. 1976; Vršnak et al. 2007; Rotter et al. 2012; Hofmeister et al. 2018). Changes in the photospheric magnetic field underlying a CH have consequences in the coronal expansion, hence, in its observed area and intensity, which shapes the solar wind outflow and its signatures at 1 au (Wang & Sheeley 1990; Gosling 1996). However, as observations are usually limited to single-point observations from Earth-view, little is known about the short-term evolution of CHs and effects on their in situ signatures.

To increase the temporal resolution and to obtain additional details about the short-term evolution of a CH, we investigate combined data from the *Solar Dynamics Observatory* (*SDO*; Pesnell et al. 2012) and the *Solar TErrestrial RElations Observatories* (*STEREO*; Kaiser et al. 2008). Around the year 2012, the two spacecraft (*STEREO-A*, and *STEREO-B*) were separated with each other and with *SDO* by 120° (Figure 1). This enables us to seamlessly track a CH over 360° and to study its entire evolution from its "cradle to grave." We first
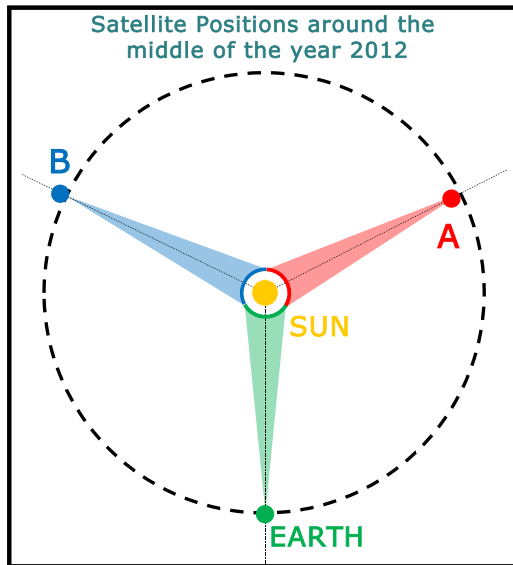
Figure 1. Schematic position of *STEREO-A*, *STEREO-B*, and Earth around the middle of the year 2012 and their estimated field of view.

investigate global CH characteristics like the CH area, intensity, orientation, and rotational patterns. The remote sensing observations are complemented by in situ measurements at the three viewpoints from *STEREO-A/-B*, the Global Geospace Science Wind satellite (Acuña et al. 1995), and the *Advanced Composition Explorer* (*ACE*; Stone et al. 1998) at a distance of about 1 au. From that, we study the CH associated solar wind plasma and magnetic field parameters.

This study is separated into two papers. The first paper investigates the CH evolution using combined EUV image data and in situ measurements from three viewpoints over 360° of the heliosphere (part I). The second paper (part II) covers the magnetic evolution of the same CH on global scales and its fine structure in terms of flux tubes. We note that part II of the study is restricted to Earth-view (*SDO*/HMI) only.

2. Methods

2.1. Data

CHs can be well observed in the emission of highly ionized elements, especially iron (e.g., Fe XII: $193/195$ Å or Fe XIV: 211 Å). Based on the high contrast between CHs and the surrounding quiet corona, the EUV wavelength of 193 Å from the Atmospheric Imaging Assembly (AIA/*SDO*) and 195 Å from the EUV Imager (EUVI/*STEREO*) is best suited to extract the CH boundaries from the different spacecraft. The observed light is emission from Fe XII ions with a peak response temperature of 1.4–$1.6 \cdot 10^6$ K (Aschwanden & Boerner 2011; Lemen et al. 2012). The data was acquired at a 1 hr cadence through the Joint Science Operations Center and the Virtual Solar Observatory (VSO).

For the in situ measurements, level 2 data for the three different viewpoints are used. For Earth position, these are the high-resolution (5 minutes) plasma and magnetic field measurements provided by OMNI https://omniweb.gsfc.nasa.gov/ and averaged over 1 hr. OMNI data is taken by different satellites (e.g., *WIND* and *ACE*) at various positions (e.g., L1) and then propagated to the Earth's Bow Shock Nose. For the two *STEREO* positions, we use 1 hr resolution solar wind magnetic field data from IMPACT (Acuña et al. 2008;

Luhmann et al. 2008) and plasma parameters from PLASTIC (Galvin et al. 2008).

2.2. EUV Image Data Reduction and Multi-instrument Intercalibration

To prepare the EUV images for multi-instrument calibration, the images were prepared to level 1.5 and 1 for *SDO* and *STEREO*, respectively, using standard SSW-IDL routines. For a common size of the images and to enhance the processing speed, full resolution images from *SDO* (4096×4096) and *STEREO* (2048×2048) were both resized to 1024×1024 pixels. In order to combine EUV image data from the different instruments, *STEREO* (195 Å) and *SDO* (193 Å) are intercalibrated following the procedure described by Caplan et al. (2016). To be able to consistently extract CH areas based on their intensity over the solar disk, an inter-instrument intensity normalization is applied and center-to-limb variations (e.g., limb-brightening in EUV) are corrected. A robust Limb-Brightening-Correction (LBC) is derived by using unbiased long-term averages of intensity bins. To correct for the different satellite orbits, instruments and instrument conditions, an Inter-Instrument-Transformation (IIT) was applied. The source code for the data based transformations (LBC, IIT) was supplied by the Predictive Science Team in MATLAB and was converted into IDL. For further information about the LBC and IIT, we refer the reader to Caplan et al. (2016).

2.3. CH Extraction and Tracking

The CH under study was chosen for reasons that were primarily based on the position of the different spacecraft. For a continuous tracking, *STEREO* and Earth-view satellites needed to be equally separated, which was only possible around the year 2012. During that time, this particular CH was outstanding, as it had a long lifespan, a reasonable size, and was located at a low-latitudinal position.

For the extraction of individual CHs on the solar disk, an intensity method with a threshold based on the median intensity of the solar disk is used. As threshold, a value of 35% of the median intensity of the solar disk was applied. Compared to the mean intensity, the median intensity is more robust and stable over time against the influence of bright and dark structures. By applying the threshold method onto EUV images, a binary map is created that is then smoothed by a median filter of 15 pixels (which equals ∼30 arcsec in the center of the solar disk) in order to remove fragments and very small dark structures and to smooth the edges of the CH. The binary map is then segmented into the different detected CHs. This threshold-based method has already been used and intensively tested by Reiss et al. (2014) and Hofmeister et al. (2017) for *SDO* images and by Rotter et al. (2012) for EIT images. To reduce projection effects when CHs are close to the limb of the solar disk (Timothy et al. 1975), CHs where the center of mass (CoM; see Section 2.4) is outside of $-45°$ and $+45°$ degrees longitude measured from the central meridian of the current spacecraft are disregarded.

The tracking of the CH under study in each image was done using a semi-automatic tracking algorithm. The CH was identified in the first image of the time series and then automatically compared to the following images. To identify the CH under study in each image, the CoM and area of all extracted CHs are compared to the forward rotated position of
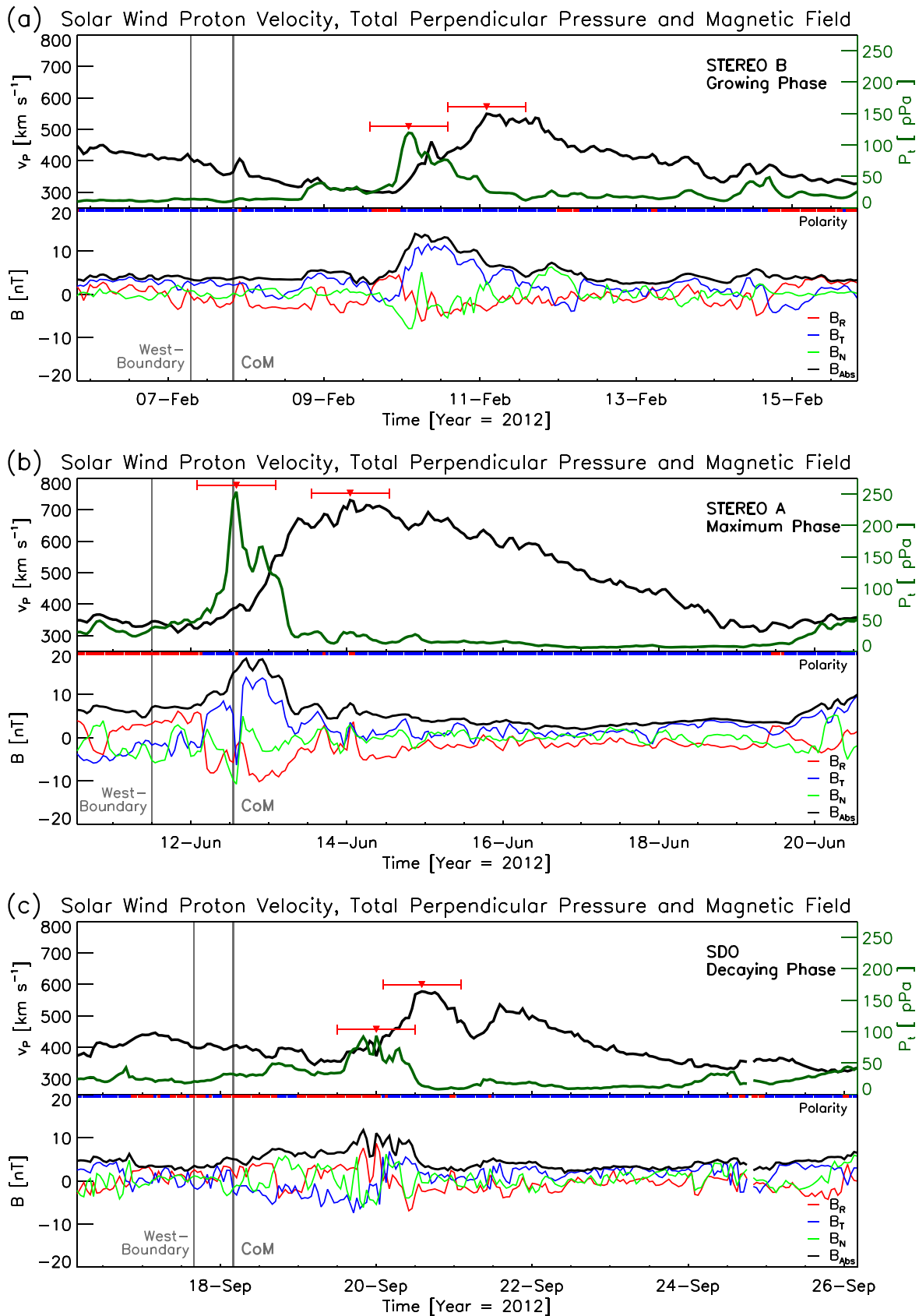
Figure 2. Examples of in situ signatures of the solar wind as observed by *STEREO-B*, *STEREO-A*, and OMNI, as the CH under study was observed near the center of the solar disk by *STEREO-B*, *STEREO-A*, and *SDO*, respectively. The panels (a)–(c) represent different stages in the CH evolution. The top panels show the solar wind bulk velocity (black) and total perpendicular pressure (green), and the bottom panels show the magnetic field components (RTN and absolute value). The red-blue bar below the velocity-pressure plot indicates the magnetic field polarity of the solar wind, with red representing positive and blue negative (=CH) polarity. The gray vertical lines are the time when the CH makes a CMP with the CoM and the west boundary. The red bars indicate the manually extracted peak (triangle) and the ±12 hr interval over which the parameter was averaged.

3

the CH in the previous image. If none or multiple similar CHs were detected, manual input was requested to identify the correct structure. This process was applied to all (>4000) images. Manual input was only needed in <5% of the images.

2.4. Analysis of CH Properties

Different CH properties, as the de-projected area, the mean intensity, the CoM, and the orientation, were calculated from the extracted binary structure. As pixels closer to the solar limb represent a larger area, the binary maps were pixel-wise corrected for the projected area on the spherical solar surface:

$$A_{i,\mathrm{corr}} = \frac{A_i}{\cos(\alpha_i)}, \qquad (1)$$

with A_i being the area per pixel and α_i the angular distance to the center of the solar disk. The total area was calculated by summing the corrected area of all CH pixels by

$$A = \sum_i^N A_{i,\mathrm{corr}}. \qquad (2)$$

The area is given in square kilometers, km^2. Using the de-projected area of the CH, the CoM is calculated pixel wise by weighing the pixels based on their area. We further calculate the longest diagonal of the CH that passes through the CoM, from which we define the orientation (ϕ) of the CH as the counterclockwise angle of its longest diagonal with respect to the solar equator. The mean intensity of the CH is calculated by

$$\bar{I} = \frac{1}{N} \sum_i^N I_i. \qquad (3)$$

With I_i being the intensity value of each CH pixel.

2.5. Solar Wind Plasma and Magnetic Field Parameters

To identify from the in situ solar wind data high-speed streams associated with the CH under study, we have to take into account the propagation time from the Sun to Earth. A CH that is centrally located on the solar disk shows a strong increase in density and magnetic field after about 1–2 days, and its peak in the solar wind plasma speed on average after 2–6 days (e.g., Vršnak et al. 2007). We therefore use the central meridian passage (CMP) of the CoM as reference and open a time-window in the in situ data set of −4 to +8 days (minus to account for E–W elongated CHs). After manually identifying the stream, the values of the solar wind plasma (peak velocity and total perpendicular pressure) and magnetic field (peak in the total magnetic field at the compression region, and magnetic field at the time when the speed peaks) were manually extracted. The total perpendicular pressure (sum of the magnetic pressure and the perpendicular plasma thermal pressure) was calculated using the formula given by Jian et al. (2006): $P_t = B^2/(2\mu_0) + \sum_j n_j kT_{\mathrm{perp},j}$, where j represents protons, electrons, and α particles. For both OMNI and *STEREO* data, we assume a constant electron temperature of 130,000 K and a constant ratio of α particles to protons of 4%. To account for the temporal extension of the stream, we averaged the in situ data of each parameter over ±12 hr around the manually extracted peak value.

Figure 2 shows three examples of the in situ data that was used. Within the defined time-window, after the marks for the CMP of the west boundary and the CoM (gray vertical lines),

Table 1
Overview of Parameters Defined in Section 2

Parameter	Definition	Description
A_{CH}	$=\sum_i A_{i,\mathrm{corr}}$	CH Area
I_{CH}	$=\frac{1}{N}\sum_i I_i$	CH Mean EUV Intensity
ϕ_{CH}		CH Orientation
v_{SW}		SW Peak Bulk Velocity
ρ_{SW}		SW Number Density
B_{SW}		SW Magnetic Field Strength
P_t	$=B^2/(2\mu_0)$	SW Total Perpendicular
	$+\sum_j n_j kT_{\mathrm{perp},j}$	Pressure
A_{SW}	$=\frac{1}{N}\sum_n A_{\mathrm{CH},n}$	Processed CH Area

we looked for typical HSS signatures using the criteria as given by Jian et al. (2009). A HSS signature can usually be identified by a pile-up of the total perpendicular pressure and a steep peak (shock) in the proton density followed by a rise in the bulk velocity that usually peaks a couple of hours/days later and then slowly decreases (upper panel). The compression affects the density, pressure, as well as the magnetic field, which usually also is sheared (lower panel). Also, the polarity of the magnetic field of the HSS must be considered, as it has to match the polarity of the source region, i.e., the CH, which is found to be negative for our event under study (see Heinemann et al. 2018). The HSS polarity was calculated using the formula given by Equation (1) in Neugebauer et al. (2002) and appears as the red and blue bar below the velocity-pressure plot. The red bars in each plot mark the manually extracted peak (triangle) and the ±12 hr interval over which the parameter was averaged. For each disk passage of the CH observed in the three different satellites (i.e., 29 disk passages in total), we extract one HSS signature with its respective properties.

Possible CME signatures in the HSS were cross-checked by using ready-catalogs maintained by Richardson & Cane[3] for *ACE* (see Richardson & Cane 2010 for a description of the catalog) and for *STEREO* from L. Jian[4] (see Jian et al. 2018, for a description of the catalog). From a total of 29 data points, we excluded 5 from the analysis: (1) 2012 March 5 because it was a CME-HSS interaction event, and the HSS signatures could not be properly separated from the CME, (2) 2012 August 5 because only a CME signature is visible, and (3) 2012 August 14, (4) 22 and (5) 2012 October 14 were excluded as no clear HSS signature could be identified associated with the CH under study.

To compare and relate the CH evolution, observed in the remote sensing data, to the in situ data, the area of the CH was processed. Based on the time of the CMP of the CoM, the area was averaged over ±18 hr ($A_{\mathrm{CH},n}$) to derive a CH area to associate with the in situ measured HSS signature (a summary of the parameters defined in Section 2 can be found in Table 1):

$$A_{\mathrm{SW}} = \frac{1}{N} \sum_n A_{\mathrm{CH},n}. \qquad (4)$$

2.6. Visualization and Correlation

To visualize the different spacecraft, the CH evolution plots show three different vertical lines. The *dashed* line marks the

---

[3] http://www.srl.caltech.edu/ACE/ASC/DATA/level3/icmetable2.htm
[4] ftp://stereodata.nascom.nasa.gov/pub/ins_data/impact/level3/STEREO_Level3_ICME.pdf

STEREO-A spacecraft, the *dashed–dotted* line *STEREO-B*, and the *dark red dashed* line *SDO*. Each of those lines represents the CMP, hence, the time when the CoM of the CH passes the central meridian of the respective spacecraft. These are featured in the Figures 7, 8(a), 9 and 10(a), (c), (d).

For correlating various parameters, the Pearson correlation coefficient and the Spearman correlation coefficient including the confidence intervals (CIs) have been calculated by boot-strapping (Efron 1979; Efron & Tibshirani 1993) the data set with over 10^5 repetitions. For each repetition, a subset with replacement was drawn from the initial set, with each data point in this subset coming from a Gaussian distribution of itself plus its standard deviation. From the resulting subset, the correlation coefficients were calculated. The given correlation coefficients are the mean values of all repetitions. The CI for the correlation coefficients (90%, 95%, 99%) were calculated using the respective quantiles (e.g., for the 95% CI the quantiles are 2.5% and 97.5%). Detailed results of the Pearson and Spearman correlation coefficients calculated for the intensity–area relation as well as the solar wind speed–area relation are reported in Table 2 which can be found in the Appendix.

3. Results on CH Properties

Figures 3–5 show an overview of the evolution (snapshots with a cadence of 9 days) of the CH at the CMP, observed in *SDO* and *STEREO* EUV image data over its entire lifespan from 2012 February 4 to October 17. An animation of the evolution is available online.

3.1. CH Area and Intensity

The CH under study became continuously detectable starting with 2012 February 3–4 after two consecutive filament eruptions that have evacuated material and opened the magnetic field lines (see Figure 6). This is observed in *STEREO-A* off-limb and in *STEREO-B* very close to the limb. Signs for the emergence of a structure of reduced intensity can already be seen before in *STEREO-A* and *SDO*; however, no continuous extraction of the structure was possible nor could we associate an HSS in the in situ data to this structure. Thus, we consider the double filament eruption event as the "formation" of the CH, and as such, it marks the start time of our analysis. Because the position of the formation of the CH is close to the solar limb, a detailed analysis of the opening process was not feasible.

Figure 7 shows the evolution of the CH area as measured from the three different spacecraft. The black line represents the calculated area from the extracted CHs, the blue line is a smoothed curve (running median of 100 images ≈4 days) to make the trend visible and to remove outliers. Extreme outliers are marked with the green roman numbers and are caused by the extraction algorithm that gives a false merging and splitting of the CH with fractions of other low-intensity areas close to the CH. From the derived profile, we find that the area evolves with a pattern that can be divided into three distinct phases.

The *growing phase* is related to an increase in area ($>6 \cdot 10^{10}$ km^2) from February until the middle of March ([1]) where the area decreases to ~$2 \cdot 10^{10}$ km^2. From the observations, we find that this decrease may be explained by interchange reconnection with a small emerging active region near the southern part of the CH and/or by overlying coronal loops and stray light from active regions nearby that obscure

the CH. After this drop, again a steady increase is observed until the area reaches the *maximum phase* ($>9 \cdot 10^{10}$ km^2) around 2012 May 13 ([2]). This maximum is very stable (with only slight variations, e.g., the dip around the start of June ([3]) that lasts until around 2012 July 03 ([4])). After the maximum,[5] we observe the *decaying phase* during which the CH area steadily declines to $< 2 \cdot 10^{10}$ km^2 ([5]) until the small CH cannot be detected anymore after 2012 October 17.

In the following, the three-phase evolution found in the area is used as a reference, and we investigate the other CH parameters in comparison to that result. Figure 8(a) shows the smoothed mean intensity together with the smoothed area. We find that the smoothed mean intensity of the CH changes by about a factor of 2.5 and that it is anti-correlated with the area evolution. The minimum of intensity corresponds with the maximum in the area. In Figure 8(b), the CH areas are plotted against their respective mean intensities. The data points of the different evolution phases are color-marked (green: growing phase, red: maximum phase, blue: decaying phase). We find a good (anti-)correlation, expressed through a Spearman correlation coefficient of −0.60 with a 95% CI of [−0.58, −0.62]. The different stages in the evolution occupy different areas in the plot, separating the phases most notably for the growing and maximum phase. The decaying phase is more scattered, showing some overlap with the growing phase.

3.2. CH Motion Patterns

Figure 9 shows different properties of the CH motion patterns. The latitudinal position over time (Figure 9(a)), the velocity of the CoM in form of the Carrington longitude (Figure 9(b)), and the CH orientation (Figure 9(c)).

The latitude of the CoM is located first in the southern hemisphere at around 20° and moves successively upwards into the northern hemisphere until the maximum phase. A subsequent slow movement toward the equator coincides with the decay of the area. During September, a fast northward movement (>25°) is derived, before the CH cannot be observed anymore. Note that the motion of the CoM carries no information of the shape and extension of the CH.

In Figure 9(b), the angular rotation speed of the CoM of the CH with respect to the Carrington rotation is shown. A constant Carrington longitude would refer to a rotation speed matching the Carrington rotation $\omega_{\mathrm{Carr}} = 14°\!.18\,\mathrm{day}^{-1}$ (Ridpath 2012). We obtain that the rotation speed changes over the lifetime of the CH (between $13°\!.7\,\mathrm{day}^{-1}$ and $14°\!.8\,\mathrm{day}^{-1}$). We observe a decrease in angular velocity until the middle of the maximum phase. There, a sudden increase in the angular velocity can be observed, which is most likely a result of the recession of the area in the northern part of the CH that causes the CoM to shift toward the equator. Thereafter, a constant angular rotation speed can be observed.

Figure 9(c) shows the change in the orientation of the CH. The orientation is defined as the counterclockwise angle of the longest CH diagonal to the equator. We find a good correspondence to the three phases as observed in the CH area, especially visible is the transition from the maximum to the decaying phase. A linear fit from 2012 February until 2012

---

[5] The transition dates for the maximum phase of the CH are based on a threshold value for the CH area of ~$6 \cdot 10^{10}$ km^2.

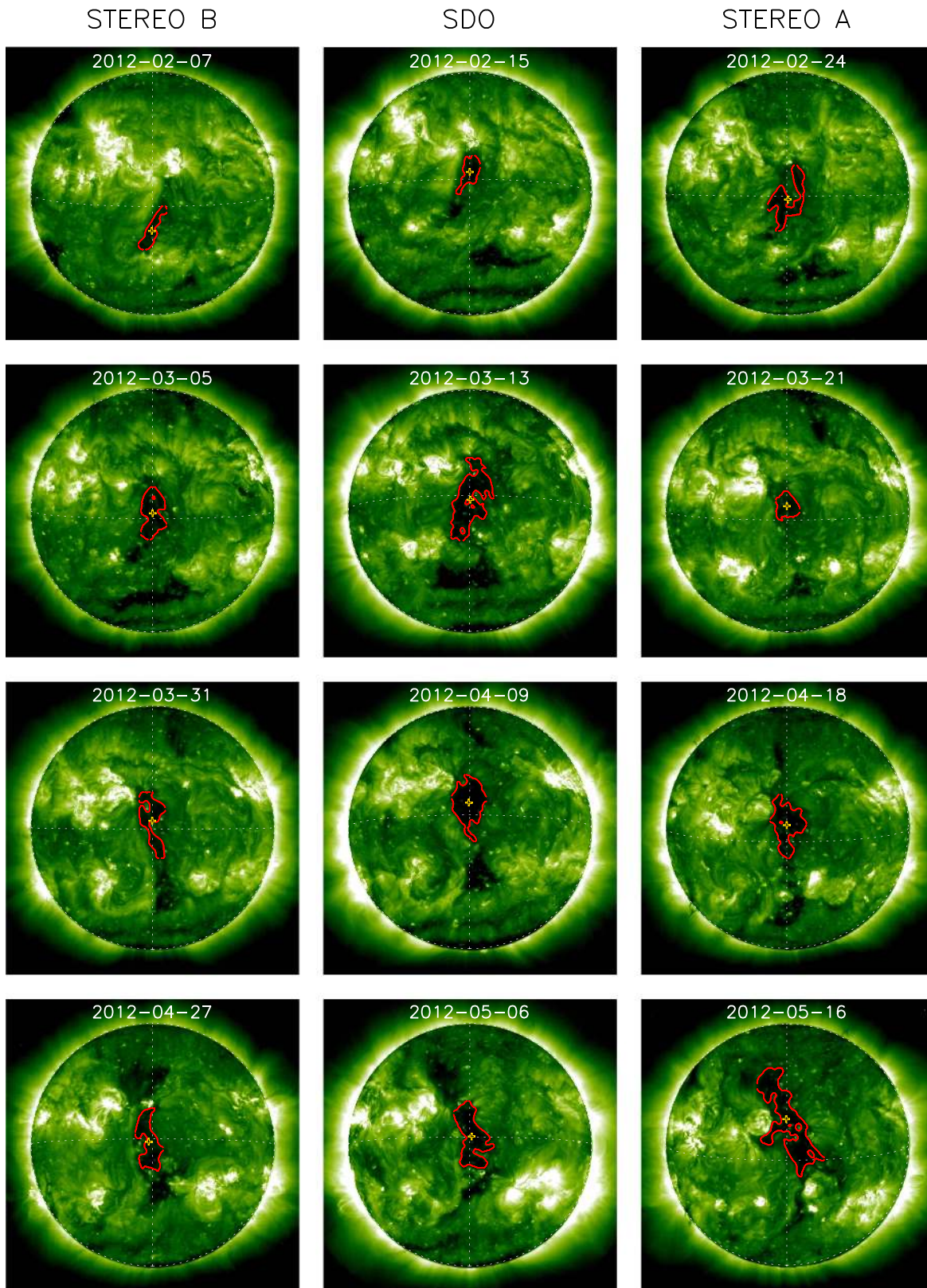STEREO B   SDO   STEREO A

Figure 3. Evolution of the CH during the time frame from 2012 February 07 to May 16. The red contours represent the boundaries of the CH. The yellow–black cross is the location of the CoM. The left panels show images taken by *STEREO-B*, the central panels are images by *SDO*, and the right panels show images by *STEREO-A*. An animation of Figures 3–5 is available online.

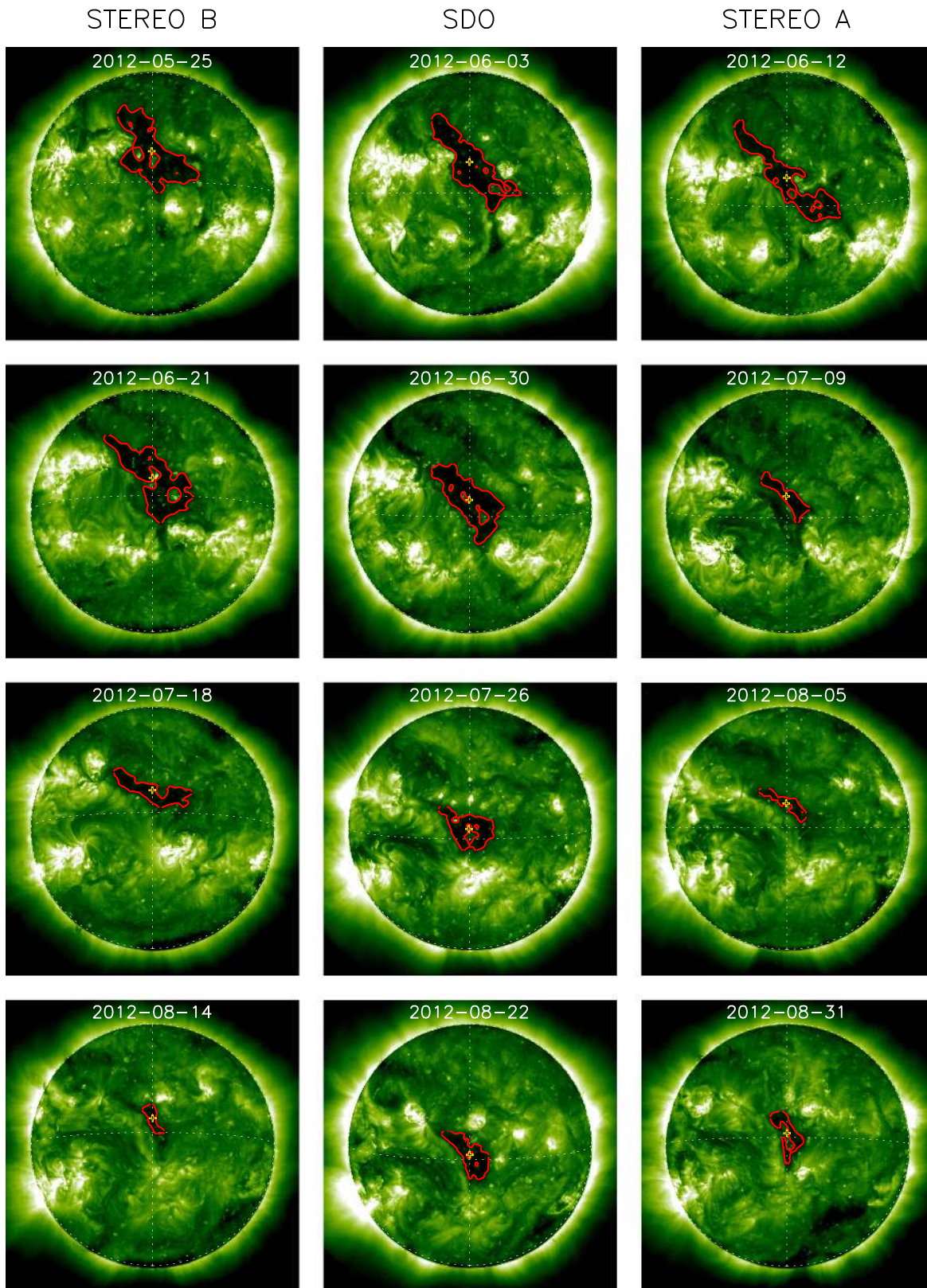(An animation of this figure is available.)

STEREO B   SDO   STEREO A

Figure 4. Same as Figure 3 but from 2012 May 25 to August 31.

July reveals a near constant counterclockwise rotation around its CoM with $0°.42 \, \mathrm{day}^{-1}$ after a starting angle of $\sim 70°$. This rotation can be observed until the end of the maximum phase; after that, coinciding with the decrease in CH area, the shape of the CH starts to become roundish. For a roundish CH, the orientation is not a well-defined parameter and therefore gives no reasonable results but causes strong fluctuations in the orientation angle derived.
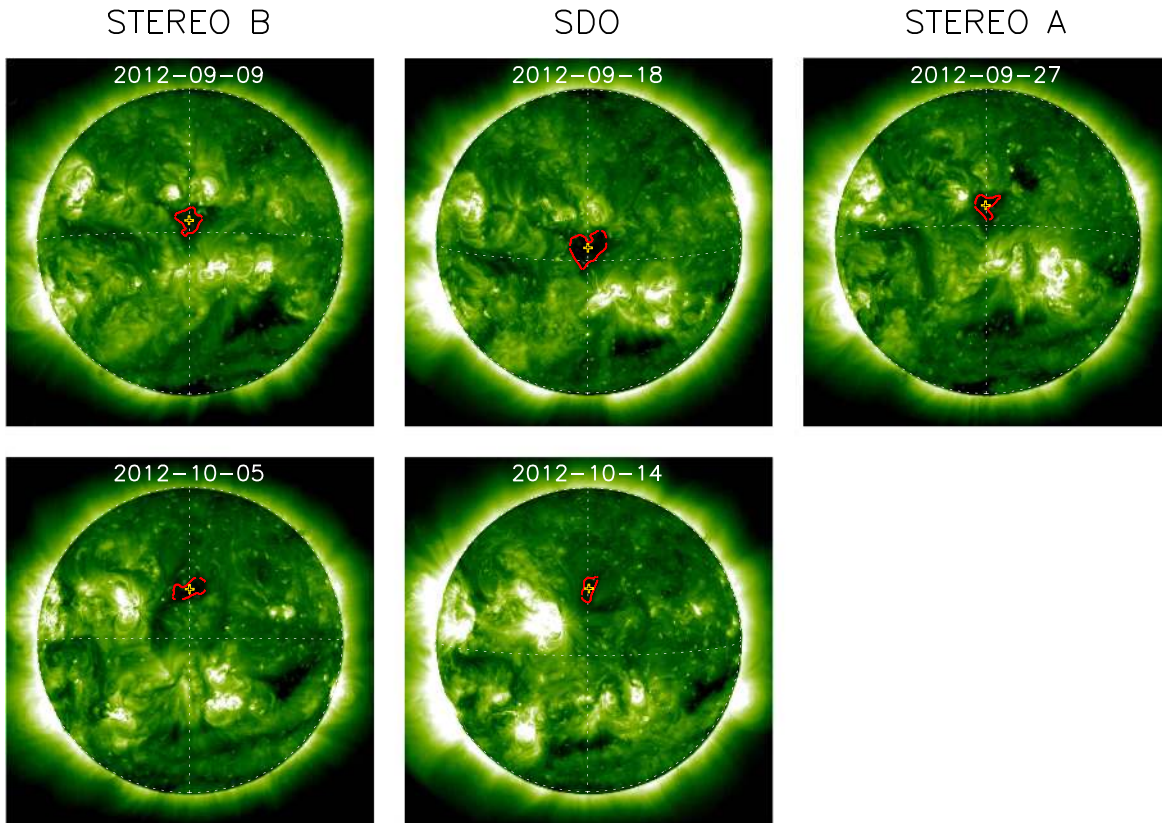
Figure 5. Same as Figure 3 but from 2012 September 09 to October 14.

4. Solar Wind Properties

Many studies already have shown that a linear relation between the CH area and the in situ measured solar wind bulk speed exists (e.g., Krieger et al. 1973; Nolte et al. 1976; Vršnak et al. 2007; Tokumaru et al. 2017; Hofmeister et al. 2018). With *STEREO*, we are able to investigate in greater detail how the different stages of CH evolution affect the solar wind properties measured at 1 au.

In Figure 10(a), the solar wind peak velocity and CH area evolution is shown. The peak velocity varies from 350 km s^{-1} during times when the CH area is small up to >700 km s^{-1} during the time of the maximum in the area. As shown in Figure 10(b) we find a strong correlation between HSS peak velocity and CH area with a Pearson correlation coefficient of 0.77 with a 95% CI of [0.57, 0.89]. The most clear relation between CH area and solar wind speed is derived for the maximum phase, whereas it is weaker for the growing and decaying phase. The decaying phase is related to a lower speed compared to the growing phase. Interestingly, CH areas during the decaying phase are related to a wide spread of speeds (350–550 km s^{-1}) while for the growing phase, we observe speeds in the range of 500–650 km s^{-1} and during the maximum phase of 600–720 km s^{-1}. Comparing our results with previous studies (Nolte et al. 1976; Tokumaru et al. 2017; Hofmeister et al. 2018), we are in good agreement with Hofmeister et al. (2018) but derive significant deviations from the slopes of the other two studies.

In Figure 10(c), the evolution of the total perpendicular pressure at the CIR compression region is shown. We find significant differences in the values between the different spacecraft, especially *STEREO-A*. However, some systematic

evolution can be derived but not in accordance with the three phases from the area evolution. At the start and end of the CH lifetime, we find lower values (20–80 pPa) than [during and] around the maximum phase from 2012 May to August (70–160 pPa).

Figure 10(d) shows the evolution of the peak magnetic field strength at the CIR compression region and at the time of the velocity peak. Similarly as for the pressure ($P_{\rm t}$), we observe an evolutionary trend of lower values for the beginning and end of the lifetime (3–10 nT and 2–5 nT respectively) and higher values from 2012 May to August (8–17 nT and 4–8 nT, respectively). However, this trend is not in accordance with the three phases from the area evolution.

5. Discussion

Using multi-viewpoint data, we have investigated the evolution of a long-lived low-latitude CH over its entire lifetime of more than 10 full solar rotations. With combined *SDO* and *STEREO* data, we could seamlessly track and investigate the evolution of the CH in EUV imagery as well as in in situ properties of the associated HSS. Our main finding is that the CH evolves in three distinct phases: the growing phase, the maximum phase, and the decaying phase.

5.1. Three-Phase Evolution

Most prominently, the three-phase evolution is derived in the CH area. The *growing phase* is mainly defined by a steady increase in area with a duration of about three months, until the transition to the *maximum phase* takes place. Compared to the other phases, the *maximum phase* is characterized by a larger
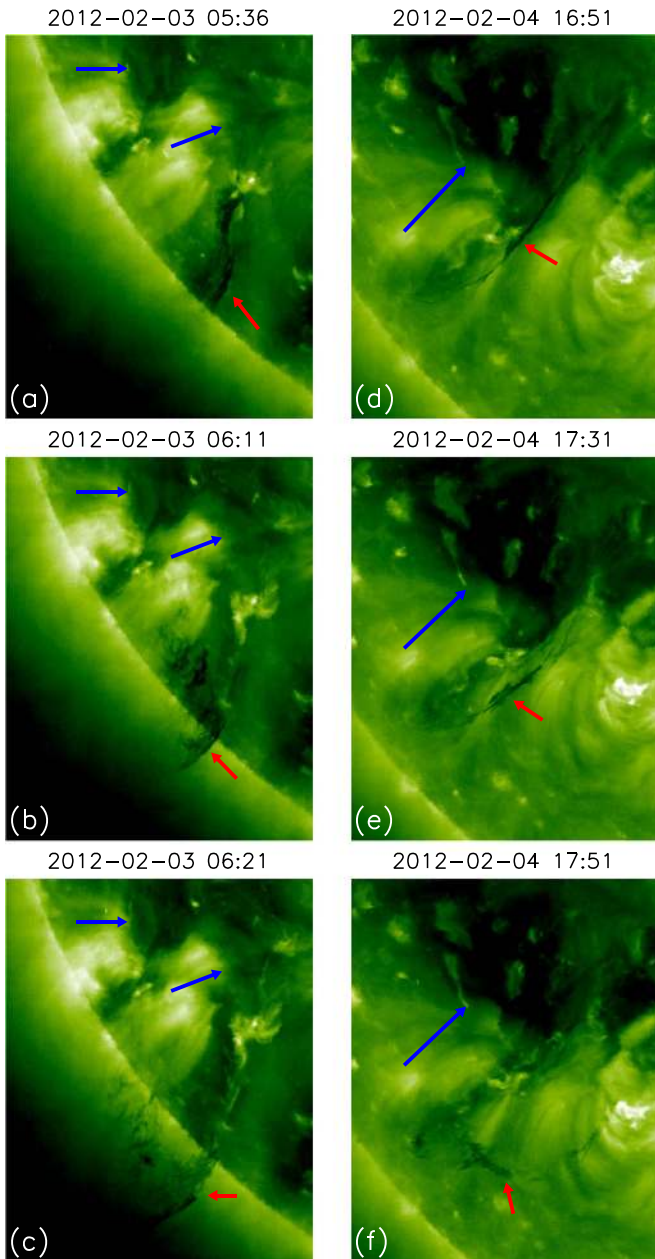
Figure 6. The formation of the CH, initiated by two filament eruptions. The red arrows point to the filament and the blue ones toward the CH that forms. Panel (a)–(c) show three snapshots in the eruption of the first filament on 2012 February 03 and panels (d)–(f) show three snapshots of the second filament eruption.

CH area (Figure 7), lower mean EUV intensity (Figure 8), a steady high solar wind speed of the associated HSS, and a stronger density/magnetic field compression of the CIR (Figure 10). The parameter values are rather stable during the *maximum phase* but only for a limited duration of around one month (the shortest of the three evolutionary phases). Around 2012 July 03, a significant drop in CH area and in situ solar wind speed heralds the last phase, the *decaying phase* in the CH lifetime. The decay continues for more than 3 months during which the CH area decreases and finally cannot be unambiguously identified anymore.

In each phase, the CH exhibits a different behavior; especially noticeable is the difference between the growing and the decaying phase. Though the CH has in both phases

similar values of area and similar solar wind plasma and magnetic field values, the solar wind plasma stream emanating from the decaying CH behaves more erratic compared to the CH growing phase. This leads us to the assumption that the physical processes that are responsible for the opening and closing of a CH have a different influence on the HSS peak velocity (see also Temmer et al. 2018).

5.2. Motional Behavior

The CH main latitudinal movement direction is northwards with a slight decrease in CoM latitude at the end of the maximum phase and the start of the decaying phase, which seems to be caused by the asymmetric (north–south direction) decline of the area (Figure 9). Structural changes of the CH, hence, changes in the CoM and its latitudinal movement, are supposed to be strongly related to the rearrangement of the global magnetic field structure (Bilenko 2002 and Bilenko & Tavastsherna 2016).

The CH main axis exhibits a counterclockwise rotation (Figure 9(c)), which might be caused by the differential rotation of the Sun acting differently on different parts of the CH. The CH is located mostly in the northern hemisphere stretching from the equator up to latitudes of $30°$ and higher. The faster rotation rates at the equator and the lower rotation rates at higher latitudes deform the CH, which becomes apparent as a counterclockwise rotation. This effect is especially noticeable when the CH has an elongated shape in the north–south direction. This finding shows that an extended CH does not rotate rigidly as a static body, but rather different parts have different rotation speeds, faster at the equator and slower at higher latitudes. A coronal differential rotation in CHs has also been found by Insley et al. (1995).

5.3. In Situ Solar Wind Plasma and Magnetic Field Signatures

Solar wind HSSs and related CIRs are a major contributor to space weather due to their recurrence and the fact that they are more predictable than impulsive, sporadic space weather events (e.g., CMEs). With the well-derived linear relation between CH areas and HSS peak speed (e.g., Nolte et al. 1976; Vršnak et al. 2007; Rotter et al. 2012; Tokumaru et al. 2017; Hofmeister et al. 2018), a forecasting seems to be straightforward. In this study, we show that these correlations are strongly related to the evolution of the CHs (Figure 10). During the growing phase, the peak velocity of the associated HSS steadily increased from $500 \, \mathrm{km \, s^{-1}}$ to $>680 \, \mathrm{km \, s^{-1}}$ in the maximum phase. With the decrease in area in the decaying phase, the speed drops to below $400 \, \mathrm{km \, s^{-1}}$. The correlation, as shown by the Pearson correlation coefficient, is 0.77 with a 95% CI of [0.57, 0.89].

From our regression analysis, we obtain a linear relation with a slope of $31.5 \pm 2.2 \, \mathrm{km \, s^{-1}}/(10^{10} \, \mathrm{km^2})$. By comparison, Tokumaru et al. (2017) derived a smaller slope with $4.31 \pm 0.15 \, \mathrm{km \, s^{-1}}/(10^{10} \, \mathrm{km^2})$ and Nolte et al. (1976) a higher slope with $80 \pm 2 \, \mathrm{km \, s^{-1}}/(10^{10} \, \mathrm{km^2})$. We are in basic agreement with the study by Hofmeister et al. (2018) with a slope of 23.2 ± 4.5 but a higher y-intercept. These strong variations in the slope in different studies may be explained by the different CH data sets used. In a recent statistical study by Hofmeister et al. (2018), a further dependence of the measured HSS speed (alternatively, of the measured slopes) on the co-latitudinal position between the spacecraft and the solar CH
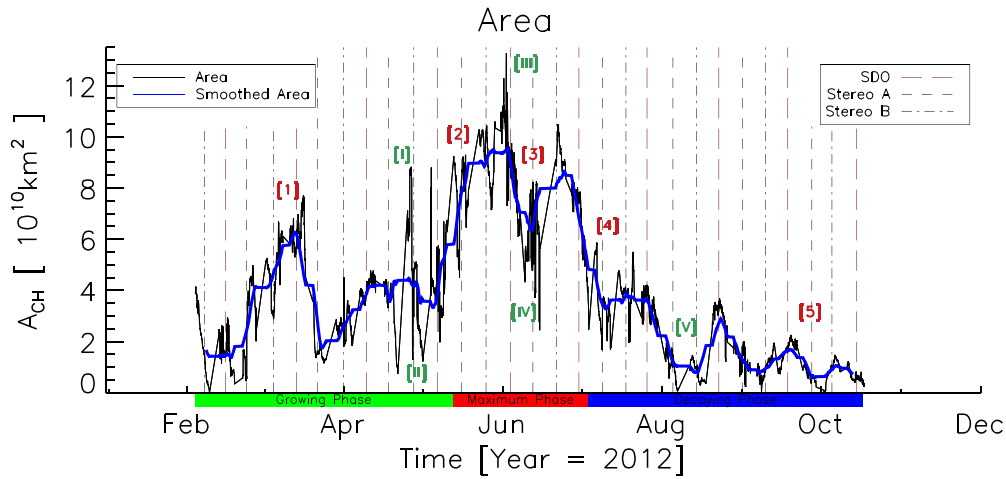
Figure 7. Evolution of the CH area (black) with smoothed curve (blue). The red numbers mark evolutionary features described in the text and the green roman numbers mark outliers. The vertical lines represent the observing spacecraft as described in Section 2.6.
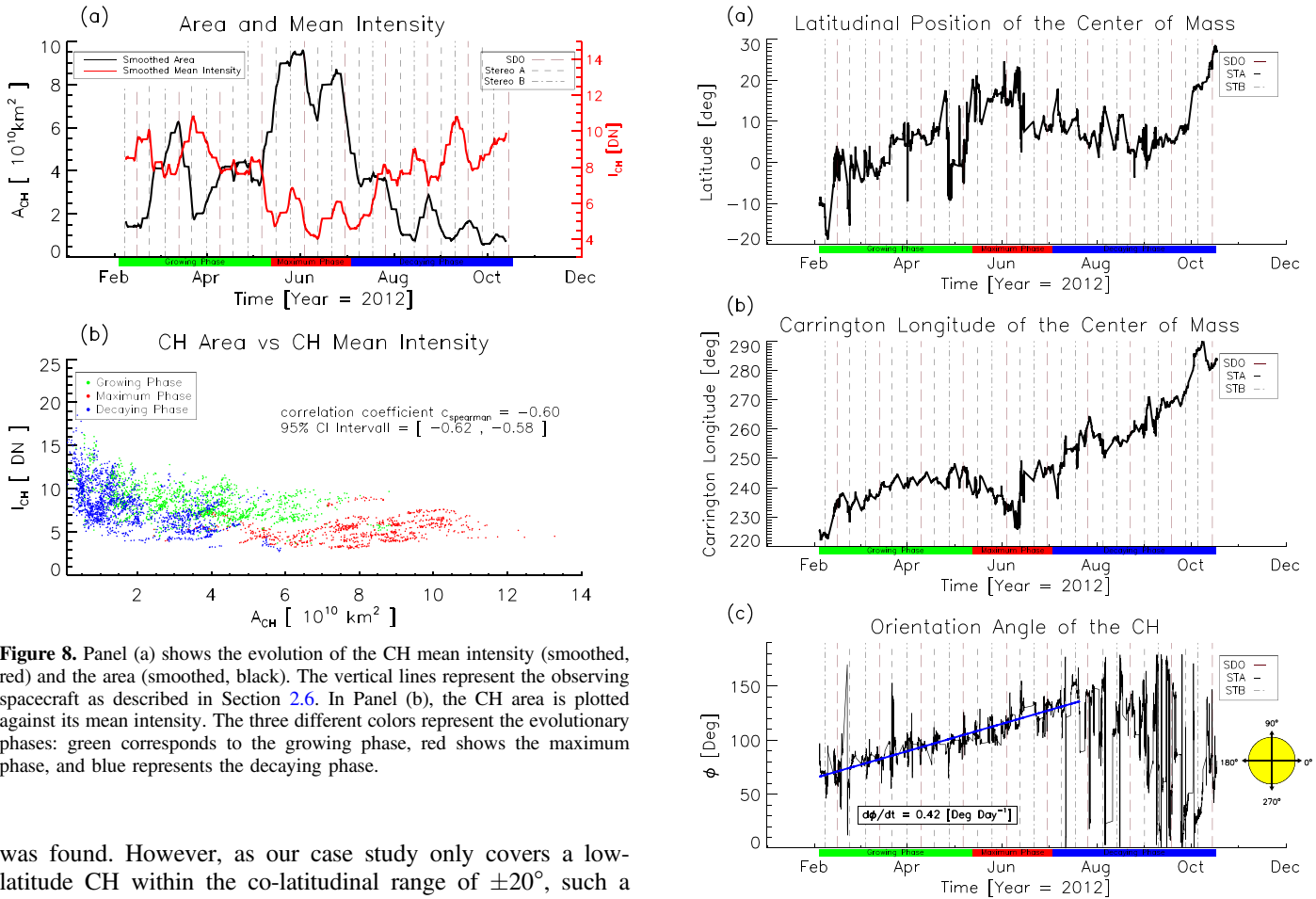

Figure 8. Panel (a) shows the evolution of the CH mean intensity (smoothed, red) and the area (smoothed, black). The vertical lines represent the observing spacecraft as described in Section 2.6. In Panel (b), the CH area is plotted against its mean intensity. The three different colors represent the evolutionary phases: green corresponds to the growing phase, red shows the maximum phase, and blue represents the decaying phase.

Figure 9. Motional behavior of the CH: (a) latitudinal movement of the CH; (b) longitudinal motion of the CH; (c) orientation angle of the CH together with a linear fit (blue) for the time where the angle can be derived unambiguously. The vertical lines in (a)–(c) represent the observing spacecraft as described in Section 2.6.

was found. However, as our case study only covers a low-latitude CH within the co-latitudinal range of $\pm 20°$, such a correlation is not visible. Studies with only near equatorial CHs are expected to yield a different slope than those covering CHs over all latitudinal ranges. This assumption also applies to this study of the evolution of one CH. Nevertheless, as could be shown here, the degree of correlation is likely dependent on the evolutionary phase of the CH. We find similar slopes during the growing and decaying phase but with different base levels (lower speed and larger spread for the decaying phase). During the maximum phase, the linear correlation is the same as the overall correlation.

The in situ measured density peak, magnetic field, and therefore total perpendicular pressure of the interaction region and the magnetic field measured at the speed peak show a general evolutionary trend, with higher values during the
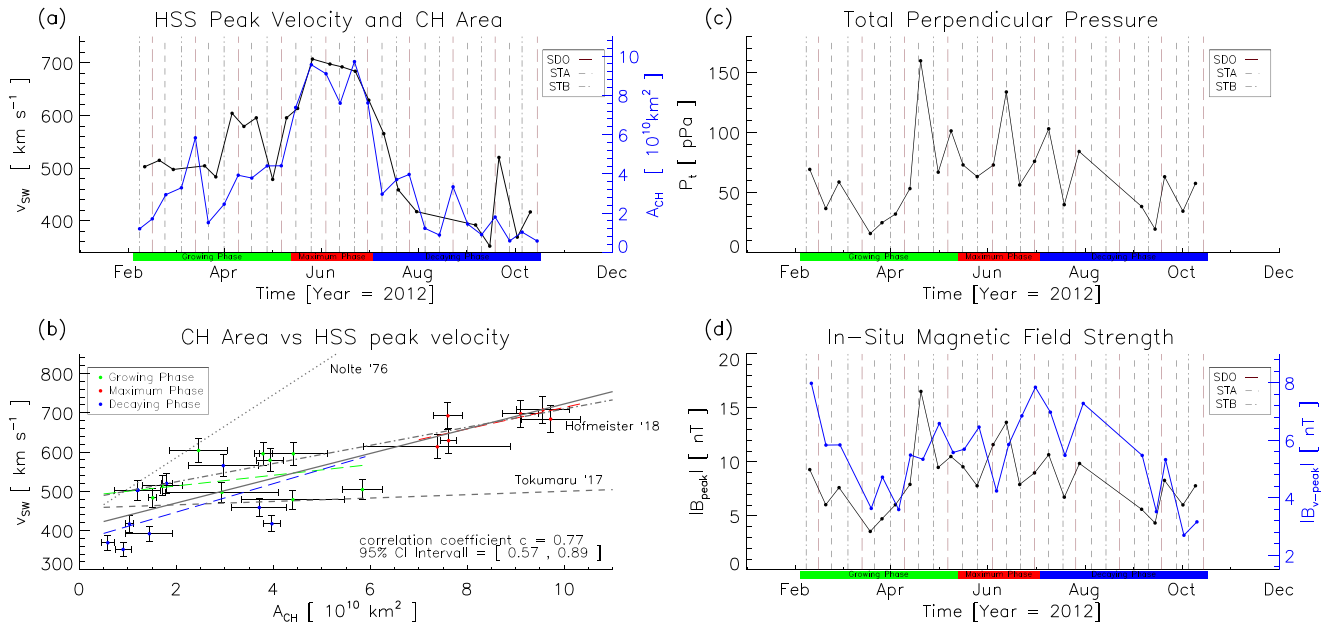
Figure 10. (a) Time evolution of the solar wind peak velocity (black) of the HSS associated with the CH together with the evolution of the CH area (blue). (b) HSS peak velocity plotted against the CH area. The three different colors represent the three different evolutionary phases (see legend). The colored lines represent a linear fit for each respective phase. The gray lines (dotted, dashed, and dashed–dotted) show relations found by the studies of Nolte et al. (1976), Tokumaru et al. (2017), and Hofmeister et al. (2018), respectively. The solid gray line represents the linear relation found in this study. (c) Total perpendicular pressure of the compression region. (d) Evolution of the peak magnetic field strength of the compression region and the magnetic field at the velocity peak. The vertical lines represent the observing spacecraft as described in Section 2.6.

maximum of the CH lifetime than during its beginning and end (Figure 10). For the total perpendicular pressure, we find large variations between the three spacecraft that may be caused by (a) instrumental effects (sensitivity, age, type) or (b) the three-dimensional structure of the HSS. However, we find no direct dependence on the co-latitude of the spacecraft to the CoM of the CH. We suppose that the plasma and magnetic field compression between fast and slow solar wind is likely influenced by the interplay between the CH structure itself (shape of the CH and its changes) and the ambient structures (nearby active regions and their activity, but also global changes in the magnetic field).

6. Summary and Conclusions

In the year 2012, the position of the two *STEREO* spacecraft combined with *SDO* provided us the unique possibility to observe and study the long-term evolution of a CH in full 360° view and the associated HSS. Our major findings are as follows:

1. We find that the CH shows a three-phase evolution consisting of the growing phase, the maximum phase, and the decaying phase. The three phases last for three, one, and more than three months, respectively. This is revealed predominantly in the evolution of the CH area but also very distinctly in its mean EUV intensity and the in situ measured solar wind speed.
2. We find an influence of the differential rotation of the Sun on the CH, as seen by the change in orientation of the CHs main axis that corresponds with different rotation rates of different CH parts, higher at the equator and lower at higher latitudes.
3. The correlation between CH area and peak solar wind speed of the associated HSS is strongest during the

maximum phase of the CH. Weaker relations are found for the growing and decaying phase. This may be related to the three-dimensional extension and propagation of the HSS, which is only measured in one specific location. Density, pressure, and magnetic field parameters of the solar wind show no distinct relation to the CH area, but we find a general evolutionary trend.

We conclude that the CH shows an evolutionary pattern with different behaviors during the three phases. During the formation of the CH until it reaches its maximum, the parameters are found to be more stable compared to the decaying process. These different physical processes most likely are related to the underlying magnetic field and affect not only the surface properties but also the outflowing plasma at a distance of 1 au. Part II of this study investigates in detail the CH underlying photospheric magnetic field from which a distinct three-phase evolution is also revealed (Heinemann et al. 2018).

Appendix

Table 2 gives detailed results of the Pearson and Spearman correlation coefficients calculated for the intensity–area relation as well as the solar wind speed–area relation. The method and calculation of the coefficients is found in Section 2.6.

Table 2
Correlation Coefficients Overview

| Relation | Figure Nr. | Pearson Correlation Coefficient | | | | |
		μ_P	σ_P	CI 90%	CI 95%	CI 99%
I_{CH} versus A_{CH}	8(b)	−0.57	0.01	[−0.56, −0.58]	[−0.56, −0.59]	[−0.55, −0.59]
v_{SW} versus A_{SW}	10(b)	0.77	0.08	[0.61, 0.87]	[0.57, 0.89]	[0.46, 0.91]

| Relation | Figure Nr. | Spearman Correlation Coefficient | | | | |
		μ_S	σ_S	CI 90%	CI 95%	CI 99%
I_{CH} versus A_{CH}	8(b)	−0.60	0.01	[−0.58, −0.62]	[−0.58, −0.62]	[−0.57, −0.62]
v_{SW} versus A_{SW}	10(b)	0.72	0.12	[0.49, 0.88]	[0.43, 0.89]	[0.30, 0.92]

ORCID iDs

Stephan G. Heinemann ⓘ https://orcid.org/0000-0002-2655-2108
Manuela Temmer ⓘ https://orcid.org/0000-0003-4867-7558
Stefan J. Hofmeister ⓘ https://orcid.org/0000-0001-7662-1960
Astrid M. Veronig ⓘ https://orcid.org/0000-0003-2073-002X

References

Acuña, M. H., Curtis, D., Scheifele, J. L., et al. 2008, SSRv, 136, 203
Acuña, M. H., Ogilvie, K. W., Baker, D. N., et al. 1995, SSRv, 71, 5
Alves, M. V., Echer, E., & Gonzalez, W. D. 2006, JGRA, 111, A07S05
Aschwanden, M. J., & Boerner, P. 2011, ApJ, 732, 81
Bilenko, I. A. 2002, A&A, 396, 657
Bilenko, I. A., & Tavastsherna, K. S. 2016, SoPh, 291, 2329
Caplan, R. M., Downs, C., & Linker, J. A. 2016, ApJ, 823, 53
Efron, B. 1979, AnSta, 7, 1
Efron, B., & Tibshirani, R. J. 1993, An Introduction to the Bootstrap (New York: Chapman and Hall)
Galvin, A. B., Kistler, L. M., Popecki, M. A., et al. 2008, SSRv, 136, 437
Gosling, J. T. 1996, ARA&A, 34, 35
Gressl, C., Veronig, A. M., Temmer, M., et al. 2014, SoPh, 289, 1783
Heinemann, S. G., Hofmeister, S. J., Veronig, A. M., & Temmer, M. 2018, ApJ, in press (arXiv:1806.10052)
Hofmeister, S., Veronig, A., Temmer, M., et al. 2018, JGRA, 123, 1738
Hofmeister, S. J., Veronig, A., Reiss, M. A., et al. 2017, ApJ, 835, 268
Insley, J. E., Moore, V., & Harrison, R. A. 1995, SoPh, 160, 1
Jian, L., Russell, C. T., Luhmann, J. G., & Skoug, R. M. 2006, SoPh, 239, 337
Jian, L. K., MacNeice, P. J., Taktakishvili, A., et al. 2015, SpWea, 13, 316
Jian, L. K., Russell, C. T., Luhmann, J. G., & Galvin, A. B. 2018, ApJ, 855, 114
Jian, L. K., Russell, C. T., Luhmann, J. G., Galvin, A. B., & MacNeice, P. J. 2009, SoPh, 259, 345
Kaiser, M. L., Kucera, T. A., Davila, J. M., et al. 2008, SSRv, 136, 5
Kilpua, E. K. J., Balogh, A., von Steiger, R., & Liu, Y. D. 2017, SSRv, 212, 1271
Krieger, A. S., Timothy, A. F., & Roelof, E. C. 1973, SoPh, 29, 505
Krista, L. D., & Gallagher, P. T. 2009, SoPh, 256, 87
Lemen, J. R., Title, A. M., Akin, D. J., et al. 2012, SoPh, 275, 17
Luhmann, J. G., Curtis, D. W., Schroeder, P., et al. 2008, SSRv, 136, 117
Neugebauer, M., Liewer, P. C., Smith, E. J., Skoug, R. M., & Zurbuchen, T. H. 2002, JGRA, 107, 1488
Nolte, J. T., Krieger, A. S., Timothy, A. F., et al. 1976, SoPh, 46, 303
Pesnell, W. D., Thompson, B. J., & Chamberlin, P. C. 2012, SoPh, 275, 3
Reiss, M., Temmer, M., Rotter, T., Hofmeister, S. J., & Veronig, A. M. 2014, CEAB, 38, 95
Richardson, I. G., & Cane, H. V. 2010, SoPh, 264, 189
Ridpath, I. 2012, A Dictionary of Astronomy (2nd rev. ed.; Oxford: Oxford Univ. Press)
Rotter, T., Veronig, A. M., Temmer, M., & Vršnak, B. 2012, SoPh, 281, 793
Schwenn, R. 2006, SSRv, 124, 51
Stone, E. C., Frandsen, A. M., Mewaldt, R. A., et al. 1998, SSRv, 86, 1
Temmer, M., Hinterreiter, J., & Reiss, M. A. 2018, JSWSC, 8, A18
Timothy, A. F., Krieger, A. S., & Vaiana, G. S. 1975, SoPh, 42, 135
Tokumaru, M., Satonaka, D., Fujiki, K., Hayashi, K., & Hakamada, K. 2017, SoPh, 292, 41
Verbanac, G., Vršnak, B., Živković, S., et al. 2011, A&A, 533, A49
Vršnak, B., Temmer, M., & Veronig, A. M. 2007, SoPh, 240, 315
Wang, Y.-M., & Sheeley, N. R., Jr. 1990, ApJ, 355, 726
Wilcox, J. M. 1968, SSRv, 8, 258